

# Enhanced strength and ductility in a high-entropy alloy via ordered oxygen complexes

Zhifeng Lei<sup>1,10</sup>, Xiongjun Liu<sup>1,10</sup>, Yuan Wu<sup>1,10</sup>, Hui Wang<sup>1</sup>, Suihe Jiang<sup>1</sup>, Shudao Wang<sup>1</sup>, Xidong Hui<sup>1</sup>, Yidong Wu<sup>1</sup>, Baptiste Gault<sup>2</sup>, Paraskevas Kontis<sup>2</sup>, Dierk Raabe<sup>2</sup>, Lin Gu<sup>3</sup>, Qinghua Zhang<sup>3</sup>, Houwen Chen<sup>4</sup>, Hongtao Wang<sup>5</sup>, Jiabin Liu<sup>6</sup>, Ke An<sup>7</sup>, Qiaoshi Zeng<sup>8</sup>, Tai-Gang Nie<sup>9</sup> & Zhaoping Lu<sup>1\*</sup>

Oxygen, one of the most abundant elements on Earth, often forms an undesired interstitial impurity or ceramic phase (such as an oxide particle) in metallic materials. Even when it adds strength, oxygen doping renders metals brittle<sup>1–3</sup>. Here we show that oxygen can take the form of ordered oxygen complexes, a state in between oxide particles and frequently occurring random interstitials. Unlike traditional interstitial strengthening<sup>4,5</sup>, such ordered interstitial complexes lead to unprecedented enhancement in both strength and ductility in compositionally complex solid solutions, the so-called high-entropy alloys (HEAs)<sup>6–10</sup>. The tensile strength is enhanced (by  $48.5 \pm 1.8$  per cent) and ductility is substantially improved (by  $95.2 \pm 8.1$  per cent) when doping a model TiZrHfNb HEA with 2.0 atomic per cent oxygen, thus breaking the long-standing strength–ductility trade-off<sup>11</sup>. The oxygen complexes are ordered nanoscale regions within the HEA characterized by (O, Zr, Ti)-rich atomic complexes whose formation is promoted by the existence of chemical short-range ordering among some of the substitutional matrix elements in the HEAs. Carbon has been reported to improve strength and ductility simultaneously in face-centred cubic HEAs<sup>12</sup>, by lowering the stacking fault energy and increasing the lattice friction stress. By contrast, the ordered interstitial complexes described here change the dislocation shear mode from planar slip to wavy slip, and promote double cross-slip and thus dislocation multiplication through the formation of Frank–Read sources (a mechanism explaining the generation of multiple dislocations) during deformation. This ordered interstitial complex-mediated strain-hardening mechanism should be particularly useful in Ti-, Zr- and Hf-containing alloys, in which interstitial elements are highly undesirable owing to their embrittlement effects, and in alloys where tuning the stacking fault energy and exploiting athermal transformations<sup>13</sup> do not lead to property enhancement. These results provide insight into the role of interstitial solid solutions and associated ordering strengthening mechanisms in metallic materials.

We studied the base alloy TiZrHfNb, the optimally oxygen-doped variant (TiZrHfNb)<sub>98</sub>O<sub>2</sub> (hereafter denoted as O-2 HEA) and for comparison also an interstitial variant with 2.0 at% nitrogen (at%, atomic per cent), that is, (TiZrHfNb)<sub>98</sub>N<sub>2</sub>, hereafter referred to as N-2 HEA. Figure 1a shows the true tensile stress–strain curves of these three as-cast HEAs. A strong strengthening effect is observed for both the oxygen- and the nitrogen-doped HEAs: the yield strength  $\sigma_y$  increases from  $0.75 \pm 0.03$  GPa for the base HEA to  $1.11 \pm 0.03$  and  $1.30 \pm 0.02$  GPa for the doped O-2 and N-2 HEAs, respectively. As expected from conventional interstitial strengthening, the ductility of the N-2 HEA is reduced, as indicated by the blue curve in Fig. 1a. Surprisingly, addition of 2.0 at% oxygen to the TiZrHfNb base HEA simultaneously improves

strength and ductility, as revealed by the red curve in Fig. 1a. The elongation has nearly doubled, increasing from  $14.21\% \pm 1.09\%$  for the base HEA to  $27.66\% \pm 1.13\%$  for the O-2 HEA, accompanied by a substantial work-hardening effect. We also observe a distinct yield point effect in the stress–strain curve of this specific alloy, which contrasts with the base and N-2 HEAs. This yield point phenomenon is similar to that observed also for many steels with solute carbon<sup>14</sup>, and results here from the interaction between oxygen and the dislocations. The O-2 HEA also exhibits a much higher work-hardening rate than the other two alloys (see inset in Fig. 1a), and the calculated hardening coefficient of the O-2 HEA is 0.124, which is much higher than that of the base HEA (0.042) and N-2 HEA (0.011), enabling the material's unexpected drastic increase in ductility. Figure 1b visualizes the anomalous interstitial strengthening behaviour of the O-2 HEA with respect to a number of established alloys<sup>15–23</sup> and the N-2 HEA, revealing that its enormous increase in strength is not achieved at the expense of ductility. We note that the mechanical properties of the current TiZrHfNb are strongly dependent on the specific concentration of oxygen. Addition of more than 3.0 at% oxygen leads to deterioration of the mechanical properties, although oxides are still not formed.

To reveal the underlying mechanism of this anomalous interstitial solid-solution strengthening effect associated with oxygen in this material, we studied the underlying nanostructures in detail down to the atomic scale. Figure 2a shows the synchrotron high-energy X-ray diffraction (XRD) patterns of the base HEA as well as for the two alloy variants O-2 and N-2 HEAs, revealing that addition of either oxygen or nitrogen atoms into the base HEA has not changed its single-phase body-centred cubic (b.c.c.) structure. This observation is also confirmed by electron back-scattering diffraction mapping. The average grain size is similar for all three alloys (Fig. 2b), that is, the changes in mechanical behaviour are not due to the Hall–Petch or size effects. Figure 2c shows an aberration-corrected scanning transmission electron microscope high-angle annular dark field (STEM-HAADF) micrograph of the O-2 HEA with the incident electron beam aligned along the  $[011]_{\text{b.c.c.}}$  zone axis of the grain selected. The Z-contrast image (where Z is the atomic number) is highly sensitive to local variations in the atomic number of the constituent elements<sup>24</sup>, that is, light atoms exhibit dark contrast, whereas heavy atoms are imaged bright. The Z-contrast of the STEM-HAADF image reveals the existence of regions enriched in light atoms (that is, (Ti, Zr)-rich) and regions enriched in heavy atoms (that is, (Nb, Hf)-rich), highlighted by red and yellow squares, respectively, in Fig. 2d. This observation reveals the formation of compositionally short-range-ordered zones of metallic elements in the O-2 HEA. Similar zones also appear in the STEM images of the base and the N-2 HEAs (see Extended Data Fig. 1), confirming that such chemical short-range ordering among the metallic matrix elements is

<sup>1</sup>Beijing Advanced Innovation Center for Materials Genome Engineering, State Key Laboratory for Advanced Metals and Materials, University of Science and Technology Beijing, Beijing, China.

<sup>2</sup>Department of Microstructure Physics and Alloy Design, Max-Planck-Institut für Eisenforschung, Düsseldorf, Germany. <sup>3</sup>Beijing National Laboratory for Condensed Matter Physics, Institute of Physics, Chinese Academy of Sciences, Beijing, China. <sup>4</sup>College of Materials Science and Engineering, Chongqing University, Chongqing, China. <sup>5</sup>Institute of Applied Mechanics, Zhejiang University, Hangzhou, China. <sup>6</sup>School of Materials Science and Engineering, Zhejiang University, Hangzhou, China. <sup>7</sup>Spallation Neutron Source, Oak Ridge National Laboratory, Oak Ridge, TN, USA. <sup>8</sup>Center for High Pressure Science and Technology Advanced Research, Pudong, Shanghai, China. <sup>9</sup>Department of Materials Science and Engineering, University of Tennessee, Oak Ridge, TN, USA. <sup>10</sup>These authors contributed equally: Zhifeng Lei, Xiongjun Liu, Yuan Wu. \*e-mail: luzp@ustb.edu.cn

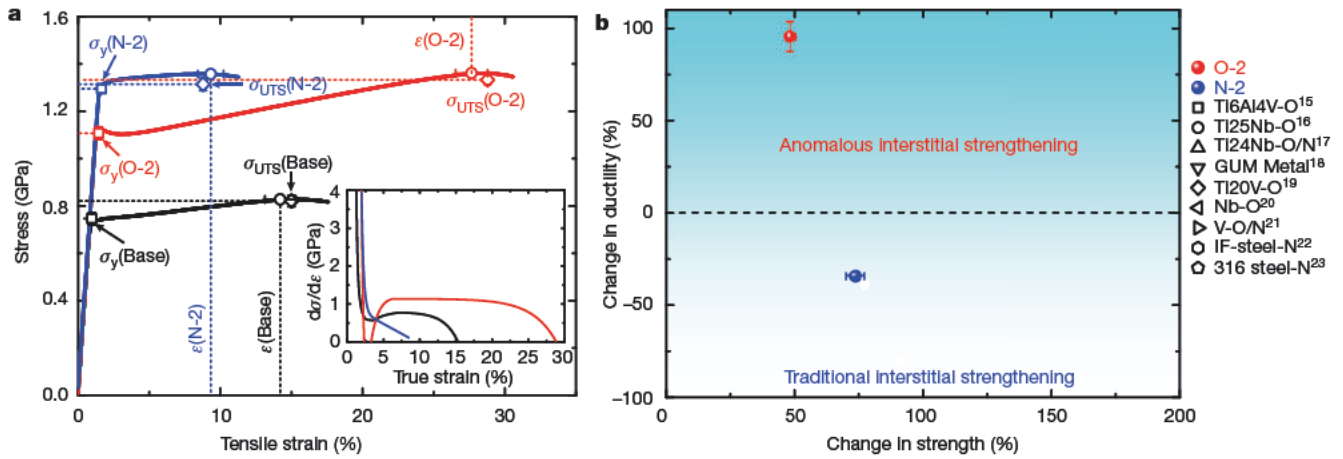


**Fig. 1 | Mechanical properties.** **a**, Room-temperature tensile stress-strain curves for the as-cast TiZrHfNb (denoted as base alloy), (TiZrHfNb)<sub>98</sub>O<sub>2</sub> (denoted as O-2) and (TiZrHfNb)<sub>98</sub>N<sub>2</sub> (denoted as N-2) HEAs.  $\sigma_y$  is the yield strength (squares),  $\sigma_{UTS}$  is the ultimate strength (diamonds) and  $\epsilon$  is the elongation (circles). The inset shows the corresponding strain-hardening response ( $d\sigma/d\epsilon$ ). A higher work-hardening rate is observed for the O-2 HEA variant (TiZrHfNb)<sub>98</sub>O<sub>2</sub> compared to the base HEA

TiZrHfNb and the N-2 HEA (TiZrHfNb)<sub>98</sub>N<sub>2</sub>. **b**, Changes in strength and ductility observed for the HEAs introduced here, relative to several types of established high-performance alloys. The reference systems are Ti6Al4V<sup>15</sup>,  $\beta$ -Ti alloys<sup>16–19</sup>, niobium<sup>20</sup>, vanadium<sup>21</sup>, interstitial free steel<sup>22</sup> and 316 austenitic stainless steels<sup>23</sup>. The alloys' interstitial oxygen or nitrogen content is indicated for comparison. The error bars are standard deviations of the mean.

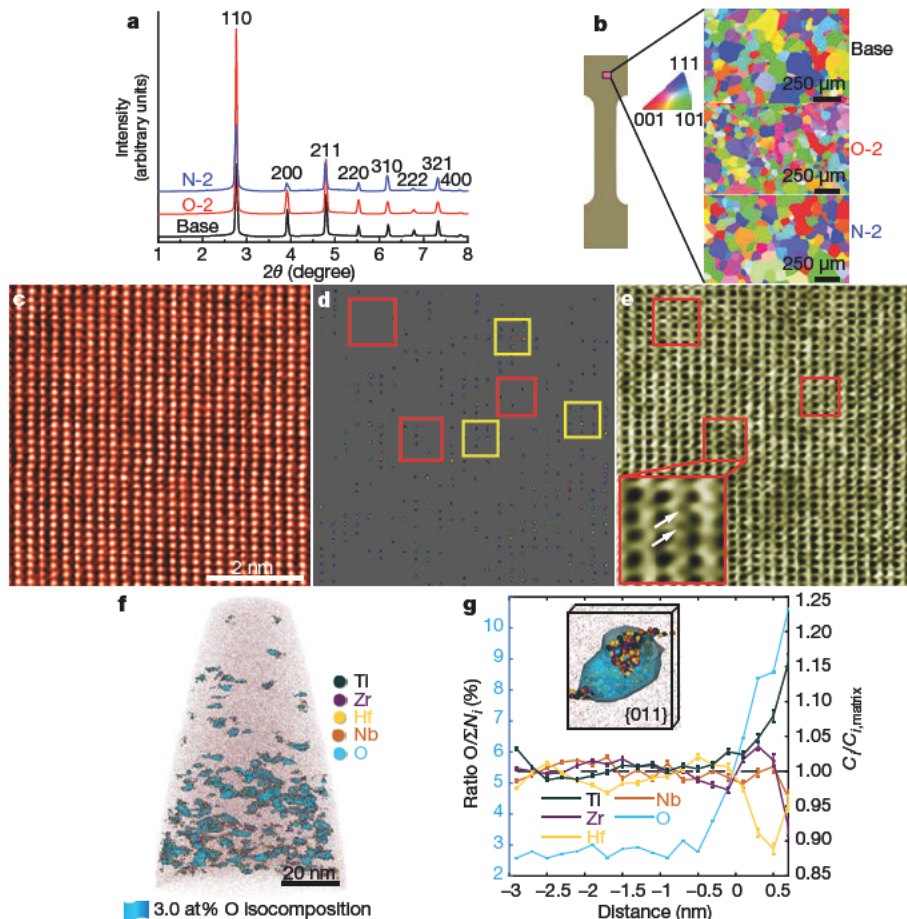


**Fig. 2 | Microscopic structure.** **a**, **b**, Synchrotron high-energy XRD and the corresponding electron back-scattering diffraction patterns of the as-cast equiatomic TiZrHfNb and the interstitially doped solid-solution HEAs. All the as-cast HEAs have single b.c.c. lattice structure. **c–e**, STEM-HAADF images for the [011]<sub>b.c.c.</sub> crystal axis with differently adjusted contrast to reveal the existence of chemical short-range ordering in the O-2 HEA (TiZrHfNb)<sub>98</sub>O<sub>2</sub>, and the corresponding STEM-ABF image that reveals the ordered oxygen complexes (OOCs). Red squares represent the Zr/Ti-rich regions and yellow squares indicate the Hf/Nb-rich regions. The inset in **e** is an enlarged view of the OOCs, with the white arrows indicating the positions of the oxygen atom columns. **f**, Atom probe

tomography three-dimensional reconstruction from the analysis of a specimen from the O-2 HEA. The threshold for the iso-composition surface is 3.0 at% O, highlighting the presence of OOCs. **g**, O composition profile as a function of the distance to the interface for a selection of particles (left axis) and evolution of the composition of the main constituents relative to their respective matrix composition (right axis). The inset shows a close-up of one such OOC, along with the {011} atomic plane imaged within the reconstruction.  $N_i$  is the number of the  $i$ th atom, while  $C_i$  and  $C_{i, \text{matrix}}$  are the concentrations of the  $i$ th atom in the OOCs and in the matrix, respectively. The error bars are standard deviations of the mean.



an intrinsic feature of these HEAs. The aberration-corrected STEM-ABF (annular bright field) image (Fig. 2e) also shows that oxygen occupies with similar frequency both the tetrahedral and the octahedral interstitial sites in the b.c.c. lattice. This surprising observation is in good agreement with simulations based on first-principles methods (see Extended Data Fig. 2). More interestingly, statistical analysis of the STEM-HAADF and the corresponding ABF images (Fig. 2d, e) demonstrates that oxygen tends to prefer interstitial positions adjacent to light-atom-rich (for example, Zr and Ti) lattice sites and form ordered oxygen complexes (OOCs) with a length scale of 1–3 nm and spacing of 2–4 nm, as indicated by the red squares in Fig. 2d, e. By contrast, no such selective ordering phenomenon was observed in the N-2 HEA, as shown in Extended Data Fig. 1d–f. Further atom probe tomography measurements of the O-2 HEA are shown in Fig. 2f, g. A blue surface encompassing regions of the point cloud containing more than 3.0 at% O is superimposed on the point cloud, as shown in Fig. 2f, revealing the presence of O-rich clusters within the data, corresponding to the OOCs. To ensure that these clusters are not related to random fluctuations in the solid solution, a randomized dataset was generated and an iso-composition surface with the same threshold reveals no such clusters (see Extended Data Fig. 3), further confirming that oxygen locally assumes an ordered state in the matrix. An average composition profile as a function of the distance to the isosurface (see Methods) was calculated from 12 particles of similar size. The resulting O profile is plotted in Fig. 2g, along with the composition of the main constituents relative to their composition away from the particle, that is, in the matrix, which reveals an excess of Ti and a slight enrichment in Zr within the O-rich clusters. These observations are consistent with the ABF images (Fig. 2d, e) observed by STEM-HAADF in the O-2 HEA.

To understand better the statistics of this occupation difference between oxygen and nitrogen, we conducted internal-friction measurements on both interstitial alloy variants O-2 and N-2 HEAs; see Extended Data Fig. 4. We found that the O-2 HEA shows an extra peak at low temperatures compared to the N-2 HEA. This result confirms that oxygen assumes an additional structural state, namely, in the form of OOCs, which is characterized by an individual trapping barrier, a state not observed for nitrogen.

According to a solid-solution strengthening model proposed by Fleischer<sup>25</sup>, we have calculated the tetragonal distortion  $\Delta\epsilon$  for the O-2 and N-2 HEAs and confirmed that their hardening mechanism is indeed of interstitial nature (see Methods). This elastic analysis explains the influence of both interstitial solute oxygen and nitrogen on the strength of the HEA. Yet, unlike traditional interstitial strengthening, which often embrittles alloys, the presence of oxygen simultaneously increases not only the strength but also the ductility in the current b.c.c. TiZrHfNb HEA. To understand this phenomenon associated with the presence of oxygen, ex situ XRD and in situ neutron diffraction loading experiments of all three alloys were conducted (Extended Data Fig. 5). We found that no phase transformation during deformation occurred in any of the three alloys. Also, ex situ transmission electron microscopy (TEM) and in situ TEM mechanical testing experiments confirm that deformation of the three alloys works via dislocation glide (Extended Data Fig. 6 and Supplementary Videos).

In general, dislocations are stored and arranged in ordered patterns during plastic deformation. Their motion is also patterned with two prevalent types of mesoscopic deformation modes: planar slip and wavy slip<sup>26</sup>. Continuous planar propagation of dislocations often prevails in face-centred cubic metals<sup>27–29</sup>, whereas plasticity in b.c.c. metals is strongly influenced by frequent cross-slip owing to the similarly close-packed {110} and {112} slip planes, resulting in wavy slip patterns<sup>30</sup>. To study these dislocation pattern features in more detail in the current alloys, we conducted high-resolution aberration-corrected STEM characterization of the pre-strained specimens (Fig. 3). Coplanar dislocation arrays resulting from planar slip are observed in the 8% pre-strained base alloy (see Fig. 3a). By contrast, well defined dipolar dislocation walls are developed in the 8% deformed O-2 HEA. Such substructures are usually caused by cross-slip of screw dislocations<sup>31</sup>

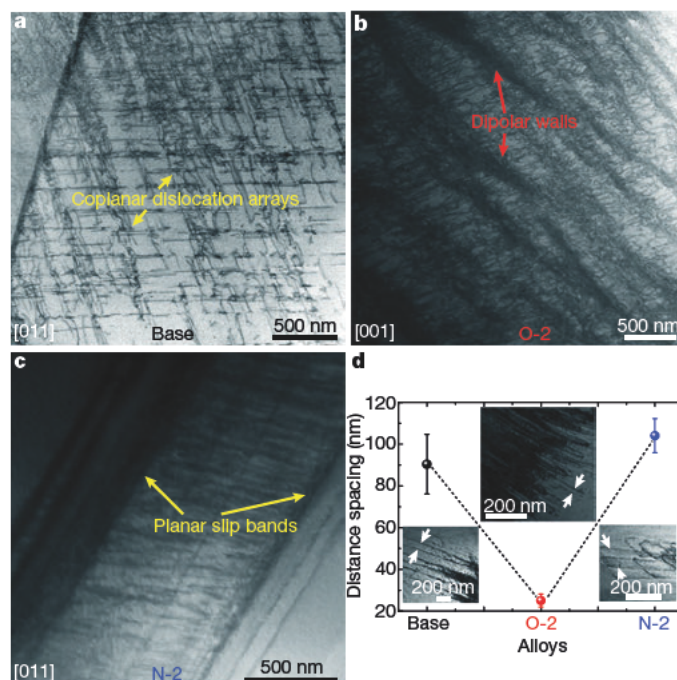


**Fig. 3 | Deformation mode.** a, STEM image of the TiZrHfNb base HEA at 8% tensile strain (the yellow arrows indicate the coplanar dislocation arrays). b, STEM image of O-2 HEA at 8% tensile strain (the red arrows indicate the dipolar walls). c, STEM image of N-2 HEA at 8% tensile strain (the yellow arrows indicate the planar slip bands). Typical planar slip is observed in the base HEA and in the nitrogen-doped alloy variant N-2 HEA. However, wavy slip dominates deformation of the oxygen-doped variant O-2 HEA, suggesting that oxygen addition leads to a plastic deformation mode dominated by wavy slip. The beam direction in a and c is [011] while that in b is [001]. d, Dislocation spacing of the TiZrHfNb base HEA and of the interstitially doped variants O-2 and N-2 HEAs probed during in situ TEM tensile experiments. The white arrows represent the dislocation spacing. The average dislocation spacing in the O-2 HEA ( $25.06 \pm 3.15$  nm) is much smaller than that in the base HEA ( $90.36 \pm 14.32$  nm) and in the N-2 HEA ( $104.06 \pm 8.14$  nm). The error bars are standard deviations of the mean.

(Fig. 3b), indicating that the plastic deformation of the O-2 HEA is dominated by wavy slip. This observation suggests that addition of oxygen facilitates cross-slip, leading to the plastic deformation mode, which is characterized not by planar slip but by wavy slip. However, for the N-2 HEA, well developed planar and banded dislocation substructures are observed (see Fig. 3c), revealing that the deformation mode is similar to that of the base HEA.

We conducted a more detailed analysis to clarify the differences in the dislocation substructures and slip band morphologies among the three HEAs formed during deformation. The experiments show that the O-2 HEA is characterized by frequent dislocation cross-slip (Extended Data Fig. 7). We also found that both the dislocation density and their velocity increase dramatically in the O-2 HEA but decrease in the N-2 variant (see Fig. 3d and Supplementary Videos 1–3). These fundamentally different dislocation multiplication, glide and patterning features further indicate that the enhanced ductility of the O-2 HEA results from facilitated cross-slip and the associated promotion of dislocation nucleation and propagation.

The key question from the substructure analysis is why the addition of interstitial oxygen not only greatly changes the dislocation patterning, motion and multiplication, but enhances the alloy's work-hardening capacity and thereby its ductility. As elaborated above, the main difference between oxygen and nitrogen in this alloy class is that oxygen occupies the interstitial sites in the Zr and/or Ti-enriched clusters in an orderly manner. By contrast, no ordered nitrogen-containing complexes are present. The nanoscale oxygen-containing complexes



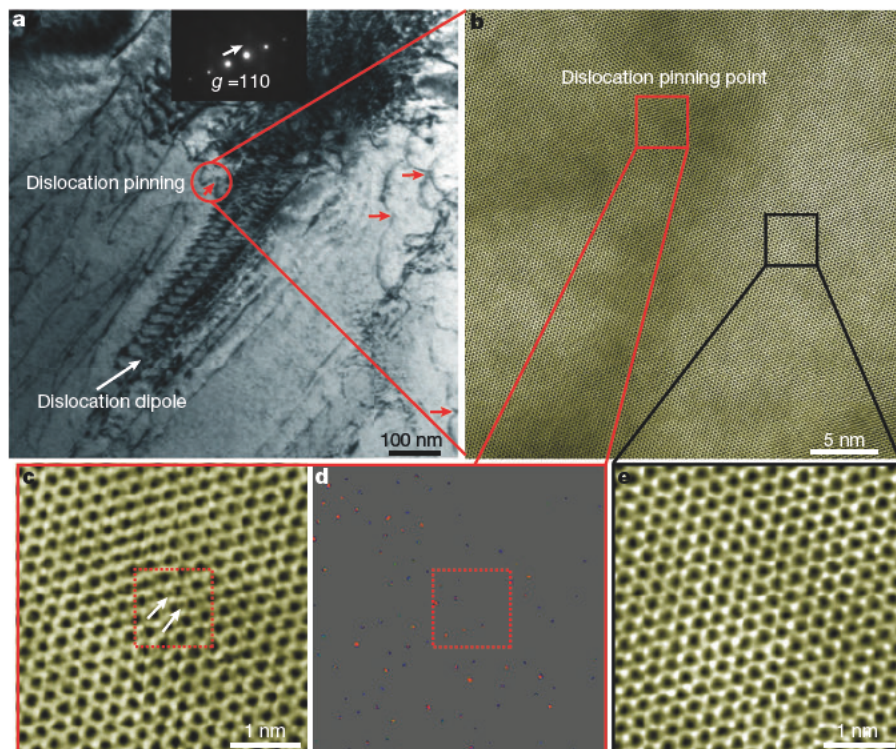


**Fig. 4 | Intrinsic mechanism.** **a**, Dislocations in the 8% strained O-2 HEA, imaged under  $\{111\}$ -type diffraction conditions. Dislocation pinning at OOCs is observed, which suppresses dislocation motion (red arrows). Also, dislocation dipoles produced by dislocation cross-slip are found (white arrow). A dislocation pinning point (red circle) at such an ordered complex was chosen for further STEM characterization in **b** and **d**.  $g$  indicates the direction of the diffraction vector. **b**, Aberration-corrected STEM-ABF image of the local atomic structure near the dislocation pinning point. Atomic structure analysis of the regions at the dislocation pinning point (red square) and away from the pinning point (black square)

were conducted. **c**, Aberration-corrected STEM-ABF image of the local atomic structure at the pinning point. The white arrows point to the oxygen atom columns around the pinned dislocation. Interstitial oxygen atoms are clearly seen in the red dotted square. **d**, Corresponding STEM-HAADF image for the  $[111]_{b.c.c.}$  crystal axis with differently adjusted contrast to reveal that the pinning effect is induced by OOCs. The red dotted zone indicates the (O, Zr, Ti)-rich region, that is, the OOC. **e**, Aberration-corrected STEM-ABF image of the local atomic structure away from the pinning point, where no similar ordered interstitial complexes were observed.

severely distort the local lattice, leading to a large strain field around them. During deformation, these OOCs interact with dislocations, that is, via pinning and promotion of dislocation double cross-slip, as revealed by STEM analyses (Extended Data Fig. 8).

To examine the interaction between OOCs and dislocations, atomic-scale structure characterization of the 8% pre-tensioned O-2 HEA was conducted by aberration-corrected STEM (Fig. 4). Dislocation dipoles produced by dislocation cross-slip and the distinct pinning effect (red arrows) of the pre-strained O-2 HEA are clearly observed (see Fig. 4a). Some of these configurations were chosen for atomic structure observation using aberration-corrected STEM-ABF imaging (Fig. 4b). Two zones, that is, the region at the dislocation pinning point (red square) and away from the point (black square), were picked out for further local atomic structure characterization, as shown in Fig. 4c–e. In the region containing the pinned dislocation, interstitial oxygen atoms are clearly observed (white arrows in Fig. 4c). The corresponding STEM-HAADF image for the  $[111]_{b.c.c.}$  crystal axis with adjusted contrast reveals oxygen atoms adjacent to Zr/Ti atoms (red dotted square in Fig. 4d). All these observations prove that the pinning of dislocations is indeed caused by OOCs. For the region away from the pinning point, no such OOCs are observed (see Fig. 4e). These results indicate that the OOCs have a twofold role during deformation: first, as dislocation pinning points similar to very small precipitates, and second, through the homogenization of the plastic flow by switching the slip mode from planar to wavy slip.

From the above analyses, the underlying deformation mechanisms responsible for the unprecedented interstitial strengthening in the O-2 HEA are schematically illustrated in Extended Data Fig. 9. In the base and N-2 HEAs, conventional substitutional clustering and

compositional short-range ordering of the metallic constituents promote planar dislocation slip. Plastic deformation in these alloys is thus topologically confined and localized to a few single-slip planes. Large dislocation densities thus assemble along the same glide planes, leading to in-plane softening and high pile-up stresses, promoting damage initiation<sup>29</sup>. In the O-2 HEA variant, however, the OOCs act on dislocations with features that lie between the effects known from conventional interstitial strengthening and those known from nano-precipitates (Extended Data Fig. 9a). During the very first stages of plastic deformation, planar slip still prevails (Extended Data Fig. 9b), but once the dislocations encounter the severely distorted, interstitial-enriched OOCs, cross-slip is promoted owing to their strong pinning effects (Extended Data Fig. 9c), resulting in massive dislocation multiplication (Extended Data Fig. 9d). Upon reaching a higher dislocation density and thus higher stress levels, dislocations also start to pass through these OOCs, promoting planar slips again until other OOCs are encountered. The interplay of sequential pinning, cutting and cross-slip leads to the homogenization of the dislocation substructure, which, on the one hand, avoids local stress peaks observed in purely planar dislocation arrays, and, on the other hand, promotes high multiplication rates of dislocation via double cross-slip and the formation of new Frank–Read sources. These features lead to high work hardening, as demonstrated in Fig. 1a. Subsequently, more and more dislocations are pinned by OOCs and dipolar walls emerge as the strain increases (Extended Data Fig. 9e), which further promotes work hardening and delays the onset of necking, eventually leading to higher ductility. For the N-2 HEA variant, we observe no such complex–dislocation dynamics and structures, that is, conventional planar dislocation slip prevails. As a result, multiplication and propagation of dislocations are limited, leading to modest ductility.

In summary, the current findings not only show how the strength–ductility trade-off can be successfully overcome for a class of HEAs, but also we elucidate a completely new type of strain-hardening mechanism based on ordered interstitial complexes. This effect enables an excellent balance between dislocation pinning, multiplication and substructure homogenization, and thereby leads to a high strain-hardening reserve and an increase in both strength and ductility. The current TiZrHfNb material in its current alloy design stage is not yet suitable for immediate utilization in high-temperature applications because of oxidation problems. Alloying with antioxidant elements, such as Al, Si and Cr, could improve the oxidation resistance of these HEAs, as has been successfully demonstrated in other types of HEAs<sup>32</sup>. We suggest that this type of ordered interstitial complex strengthening mechanism is also applicable to a wide range of other alloy classes.

## Online content

Any methods, additional references, Nature Research reporting summaries, source data, statements of data availability and associated accession codes are available at <https://doi.org/10.1038/s41586-018-0685-y>.

Received: 7 March; Accepted: 14 September 2018;

Published online: 14 November 2018

- Conrad, H. Effect of interstitial solutes on the strength and ductility of titanium. *Prog. Mater. Sci.* **26**, 123–403 (1981).
- Tyson, W. R. Strengthening of hcp Zr, Ti and Hf by interstitial solutes—a review. *Can. Metall. Q.* **6**, 301–332 (1967).
- Mouawad, B., Boulmat, X., Fabrége, D., Perez, M. & De Carlan, Y. Tailoring the microstructure and the mechanical properties of ultrafine grained high strength ferritic steels by powder metallurgy. *J. Nucl. Mater.* **465**, 54–62 (2015).
- Wei, Q. et al. Influence of oxygen content on microstructure and mechanical properties of Ti–Nb–Ta–Zr alloy. *Mater. Des.* **32**, 2934–2939 (2011).
- Ando, T., Nakashima, K., Tsuchiyama, T. & Takaki, S. Microstructure and mechanical properties of a high nitrogen titanium alloy. *Mater. Sci. Eng. A* **486**, 228–234 (2008).
- Cantor, B., Chang, I. T. H., Knight, P. & Vincent, A. J. B. Microstructural development in equiatomic multicomponent alloys. *Mater. Sci. Eng. A* **375/377**, 213–218 (2004).
- Yeh, J. W. et al. Nanostructured high-entropy alloys with multiple principal elements: novel alloy design concepts and outcomes. *Adv. Eng. Mater.* **6**, 299–303 (2004).
- Zhang, Y. et al. Microstructures and properties of high-entropy alloys. *Prog. Mater. Sci.* **61**, 1–93 (2014).
- Li, Z. M., Pradeep, K. G., Deng, Y., Raabe, D. & Tasan, C. C. Metastable high-entropy dual-phase alloys overcome the strength–ductility trade-off. *Nature* **534**, 227–230 (2016).
- Gludovatz, B. et al. A fracture resistant high entropy alloy for cryogenic applications. *Science* **345**, 1153–1158 (2014).
- Ritchie, R. O. The conflicts between strength and toughness. *Nat. Mater.* **10**, 817–822 (2011).
- Wang, Z. et al. The effect of interstitial carbon on the mechanical properties and dislocation substructure evolution in Fe<sub>40.4</sub>Ni<sub>11.3</sub>Mn<sub>34.8</sub>Al<sub>7.5</sub>Cr<sub>6</sub> high entropy alloys. *Acta Mater.* **120**, 228–239 (2016).
- Zhu, Y. T. & Liao, X. Nanostructured metals: retaining ductility. *Nat. Mater.* **3**, 351–352 (2004).
- Cottrell, A. H. & Bilby, B. A. Dislocation theory of yielding and strain ageing of iron. *Proc. Phys. Soc. A* **62**, 49 (1949).
- Oh, J. M. et al. Oxygen effects on the mechanical properties and lattice strain of Ti and Ti–6Al–4V. *Met. Mater. Int.* **17**, 733–736 (2011).
- Yin, F., Iwasaki, S., Ping, D. & Nagai, K. Snoek-type high-damping alloys realized in  $\beta$ -Ti alloys with high oxygen solid solution. *Adv. Mater.* **18**, 1541–1544 (2006).
- Ramarolahy, A. et al. Microstructure and mechanical behavior of superelastic Ti–24Nb–0.5O and Ti–24Nb–0.5N biomedical alloys. *J. Mech. Behav. Biomed. Mater.* **9**, 83–90 (2012).
- Besse, M., Castany, P. & Gloriant, T. Mechanisms of deformation in gum metal TNTZ–O and TNTZ titanium alloys: a comparative study on the oxygen influence. *Acta Mater.* **59**, 5982–5988 (2011).
- Wang, X., Li, L., Xing, H., Ou, P. & Sun, J. Role of oxygen in stress-induced  $\omega$  phase transformation and {332}<113> mechanical twinning in  $\beta$ Ti–20V alloy. *Scr. Mater.* **96**, 37–40 (2015).
- Sankar, M., Baligidad, R. G. & Gokhale, A. A. Effect of oxygen on microstructure and mechanical properties of niobium. *Mater. Sci. Eng. A* **569**, 132–136 (2013).
- Jo, M. G., Madakashira, P. P., Suh, J. Y. & Han, H. N. Effect of oxygen and nitrogen on microstructure and mechanical properties of vanadium. *Mater. Sci. Eng. A* **675**, 92–98 (2016).
- Shen, Y. Z., Oh, K. H. & Lee, D. N. Nitrogen strengthening of interstitial-free steel by nitriding in potassium nitrate salt bath. *Mater. Sci. Eng. A* **434**, 314–318 (2006).
- Talha, M., Behera, C. K. & Sinha, O. P. Effect of nitrogen and cold working on structural and mechanical behavior of Ni-free nitrogen containing austenitic stainless steels for biomedical applications. *Mater. Sci. Eng. C* **47**, 196–203 (2015).
- Pennycook, S. J., Rafferty, B. & Nellist, P. D. Z-contrast imaging in an aberration-corrected scanning transmission electron microscope. *Microsc. Microanal.* **6**, 343–352 (2000).
- Fleischer, R. L. Solution hardening by tetragonal distortions: application to irradiation hardening in FCC crystals. *Acta Metall.* **10**, 835–842 (1962).
- Hong, S. I. & Laird, C. Mechanisms of slip mode modification in F.C.C. solid solutions. *Acta Metall.* **38**, 1581–1594 (1990).
- Yao, M. J., Pradeep, K. G., Tasan, C. C. & Raabe, D. A novel, single phase, non-equiatomic FeMnNiCoCr high-entropy alloy with exceptional phase stability and tensile ductility. *Scr. Mater.* **82**, 5–8 (2013).
- Yoo, J. D. & Park, K. T. Microband-induced plasticity in a high Mn–Al–C light steel. *Mater. Sci. Eng. A* **496**, 417–424 (2008).
- Gerold, V. & Karnthaler, H. P. On the origin of planar slip in f.c.c. alloys. *Acta Metall.* **37**, 2177–2183 (1989).
- Nabarro, F. R. & Duesbery, M. S. *Dislocations in Solids* Vol. 11 (Elsevier, Amsterdam, 2002).
- Mughrabi, H., Ackermann, F. & Herz, K. *Fatigue Mechanisms ASTM STP 675* 69 (American Society for Testing Materials, Philadelphia, 1979).
- Liu, C. M., Wang, H. M., Zhang, S. Q., Tang, H. B. & Zhang, A. L. Microstructure and oxidation behavior of new refractory high entropy alloys J. *Alloys Compd.* **583**, 162–169 (2014).

**Acknowledgements** This research was supported by National Natural Science Foundation of China (grant numbers 51671018, 11790293, 51871016, 51531001 and 51671021), the 111 Project (grant number B07003), the Program for Changjiang Scholars and Innovative Research Team in University of China (grant number IRT\_14R05) and the Projects of SKLMM-USTB (grant numbers 2018Z-01 and 2018Z-19). Yuan W. acknowledges financial support from the Top-Notch Young Talents Program. Yuan W. and Hui W. acknowledges financial support from the Fundamental Research Funds for the Central Universities. We thank F. Zhang at the University of Science and Technology Beijing for help with synchrotron XRD. We also thank H. L. Huang at the University of Science and Technology Beijing and L. Qi and X. J. Zhao at the Chongqing University for help with TEM/STEM characterization and discussion.

**Author contributions** Z. Lu designed the study. Z. Lei, X.L., Yuan W., Hui W., S.J., S.W., X.H. and Yidong W. carried out the main experiments. Z. Lei, X.L., Yuan W., Z. Lu, B.G. and D.R. analysed the data and wrote the main draft of the paper. L.G., Q.Z., H.C., Hongtao W. and J.L. conducted the TEM and STEM characterizations. B.G., P.K. and D.R. prepared the atom probe tomography specimens, processed the data and interpreted the results. K.A. conducted the neutron diffraction. Q.Z. conducted the synchrotron XRD. All authors contributed to the discussion of the results, and commented on the manuscript.

**Competing interests** The authors declare no competing interests.

## Additional information

**Extended data** is available for this paper at <https://doi.org/10.1038/s41586-018-0685-y>.

**Supplementary information** is available for this paper at <https://doi.org/10.1038/s41586-018-0685-y>.

**Reprints and permissions information** is available at <http://www.nature.com/reprints>.

**Correspondence and requests for materials** should be addressed to Z.L.  
**Publisher's note:** Springer Nature remains neutral with regard to jurisdictional claims in published maps and institutional affiliations.



## METHODS

**Material preparation.** HEAs have desirable properties compared to traditional alloys with one major component<sup>33–36</sup>. Among them, HEAs consisting of metallic elements with very high melting points ( $>1,900$  K) have attracted considerable attention owing to features such as good softening resistance at elevated temperatures and slow diffusion kinetics<sup>37–39</sup>. Here, alloy ingots with a nominal composition of TiZrHfNb, (TiZrHfNb)<sub>98</sub>O<sub>2</sub> and (TiZrHfNb)<sub>98</sub>N<sub>2</sub> (at%) were prepared by arc-melting a mixture of pure metals (purity  $>99.9$  wt%), TiN (99.9 wt%) and TiO<sub>2</sub> (99.9 wt%) in a Ti-gettered high-purity argon atmosphere. The ingots were remelted at least eight times to ensure chemical homogeneity. Melted alloys were eventually drop-cast into a water-cooled copper mould with dimensions of 10 mm  $\times$  10 mm  $\times$  60 mm.

**XRD.** Synchrotron XRD patterns were obtained from each of the alloys at the Advanced Photon Source at Argonne National Laboratory, USA. Two-dimensional diffraction patterns were collected in transmission geometry using a PerkinElmer  $\alpha$ -Si flat-panel large-area detector at the 11-ID-C beam line. The wavelength of the X-ray was about 0.117418 Å, and the beam size was 500  $\times$  500  $\mu$ m<sup>2</sup>. One-dimensional XRD patterns were obtained by integrating the two-dimensional patterns with Fit 2d software (<http://www.esrf.eu/computing/scientific/FIT2D/>). Phase identification of the as-cast alloys and the deformed alloys were also conducted by XRD using Cu K $\alpha$  radiation (XRD model MXP21VAHF).

**SEM.** Microstructure and morphology were characterized by a Zeiss Supra 55 field emission scanning electron microscope equipped with an AZtecHKL electron back-scattering diffraction system. The electron back-scattering diffraction specimens were initially polished with 2,000-grit SiC paper and subsequently electrochemically polished using a 6% perchloric acid + 30% *n*-butyl alcohol + 64% methyl alcohol solution at a direct voltage of 30 V at room temperature (298 K). The tensile samples used for surface morphology observation were also electrochemically polished.

**Atom probe tomography.** Atom probe tomography analyses were carried out for the base, O-2 and N-2 HEAs in a Cameca LEAP 3000X HR under ultrahigh vacuum of approximately  $2.5 \times 10^{-11}$  torr, at a specimen temperature of 80 K, a target evaporation rate of 3 ions for 1,000 pulses on average in high-voltage pulsing mode at 15% pulse fraction. Atom probe tomography specimens were prepared by focused ion beam milling on a dual-beam FEI Helios 600 using the protocol outlined in ref. 40. The CAMECA integrated visualization and analysis software IVAS 3.6.8 was used for data processing and three-dimensional atomic reconstruction.

**Mechanical property measurements.** Room-temperature tensile properties were evaluated using a CMT4105 universal electronic tensile testing machine with an initial strain rate of  $2.0 \times 10^{-4}$  s<sup>-1</sup>. Dogbone-shaped tensile samples with a cross section of  $1.0 \times 3.0$  mm<sup>2</sup> and a gauge length of 20 mm were cut using electrical discharging. At least 5 samples were tested for each composition. Hardness measurements were conducted using a Vickers hardness tester (430SVD) with a load of 5 N for 15 s, and for each specimen, at least 15 indents were measured to obtain an average value. Nanoindentation tests were performed using the Nanoindenter XP system equipped with a spherical indenter with a radius of 1  $\mu$ m, and at least 100 indents were measured to obtain an average value of modulus. The samples for hardness measurements and nanoindentation tests were prepared by electrochemical polishing.

**In situ neutron diffraction measurements.** In situ neutron diffraction investigations upon tensile loading were conducted using a MTS load-frame on the VULCAN diffractometer, at the Spallation Neutron Source of Oak Ridge National Laboratory. VULCAN is equipped with two detector banks positioned at  $\pm 90^\circ$  diffraction angles, which are designated banks 1 and 2, respectively. An incident neutron beam of 3 mm high and 3 mm wide, together with a pair of 5 mm radial collimators, were used to define the sampling volume during the diffraction experiments. The neutron diffraction data were reduced and then analysed by single peak fitting using the VDRIVE program<sup>41</sup>.

**TEM.** Microstructure of the as-cast and fractured specimens was characterized by high-resolution TEM with a JEM-2010. In situ TEM observations were conducted with a JEM-2100 TEM equipped with a tensile loading stage. An aberration-corrected FEI Titan G260–300 kV S/TEM was used to analyse the atomic structure and morphology of the 8% pre-strained samples. The TEM specimens were first mechanically ground to 50  $\mu$ m thickness and then twin-jet electropolished using 6% perchloric acid + 30% *n*-butyl alcohol + 64% methyl alcohol solution.

**Internal-friction measurements.** Beam-shaped samples with dimensions of 1 mm  $\times$  2 mm  $\times$  (35–55) mm were used for damping-capacity measurement on a multifunctional internal-friction device (MFP-1000 at the Institute of Solid State Physics, Chinese Academy of Sciences) at low frequencies of 0.5 Hz, 1.0 Hz, 2.0 Hz and 4.0 Hz over a temperature range from 300 K to 1,000 K under continuous heating in vacuum. All samples were polished using a 2,000-grit SiC paper to eliminate surface scratches. A heating rate of 2 K min<sup>-1</sup> and a forced vibration with a strain amplitude of  $2 \times 10^{-5}$  were applied for the damping measurements. Damping data were collected using a fully automated system that measured the angular velocity of

the pendulum around the equilibrium position<sup>42</sup>. The background was subtracted according to the following equation

$$Q_b^{-1} = A + B \exp\left(\frac{-C}{kT}\right) \quad (1)$$

where  $Q_b^{-1}$  is the energy dissipation coefficient of the background, and A, B and C are the parameters to be determined after optimization of the  $\chi^2$  function<sup>43</sup>.

**Theoretical calculations and modelling.** The first-principles calculations were conducted using the density functional theory (DFT)-based Vienna ab initio simulation package (VASP)<sup>44</sup> using projector augmented waves (PAW)<sup>45</sup> and the generalized gradient approximation of Perdew–Burke–Ernzerhof (GGA-PBE)<sup>46</sup> for the exchange correlation functional. A 72-atom b.c.c.-like special quasirandom structure<sup>47</sup> supercell was constructed to model the quaternary TiZrHfNb HEA which served as the base reference alloy state. To investigate the occupation probability of oxygen or nitrogen in the HEA, we placed one interstitial atom of oxygen or nitrogen at the octahedral or tetrahedral interstitial sites, respectively, in the supercell and calculated the system energy for the case of the oxygen/nitrogen at these different interstitial sites. The occupation probability was then estimated by the statistical distribution of system energy as shown in Extended Data Fig. 2. Structural relaxations and final static calculations were performed to obtain stable structures and more accurate energy values using the conjugate gradient method<sup>48</sup> and the linear tetrahedron method including Blöchl corrections<sup>49</sup>, respectively. The energy cutoff on the wave function is taken as 450 eV, which is 1.3 times higher than the default value for all elements in this work. A  $2 \times 3 \times 3$  Monkhorst-Pack-ENREF-250 *k*-point mesh was used to sample the Brillouin zone. The energy convergence criterion for the electronic self-consistency was chosen as  $10^{-6}$  eV per atom.

**Theoretical calculations of interstitial strengthening.** Interstitials in b.c.c. metals usually produce a tetragonal distortion of the lattice. The interaction between screw dislocations and such tetragonal-distortion centres is substantial, owing to their large associated shear strains<sup>51</sup>. Generally, hardening due to tetragonal distortion fields is much larger than that for spherical distortions (for example, substitutional solid-solution strengthening). Fleischer treated solid-solution hardening by such tetragonal distortion fields as ‘rapid hardening’ and estimated the yield strength increment to be:

$$\Delta\tau = \frac{G\Delta\epsilon c^{1/2}}{3} \quad (2)$$

where  $G$  is the shear modulus,  $\Delta\epsilon$  is the difference between the longitudinal and transverse strain of the tetragonal distortion source when interstitial atoms occupy the interstitial sites in alloys, and  $c$  is the atomic concentration of interstitial atoms creating such defects. Herein we use the change of hardness  $\Delta H_v$  to quantify the effect of solid-solution strengthening<sup>52</sup>, rendering equation (2) thus:

$$\Delta H_v = 3^{3/2} \frac{G\Delta\epsilon c^{1/2}}{3} = 3^{1/2} G\Delta\epsilon c^{1/2} \quad (3)$$

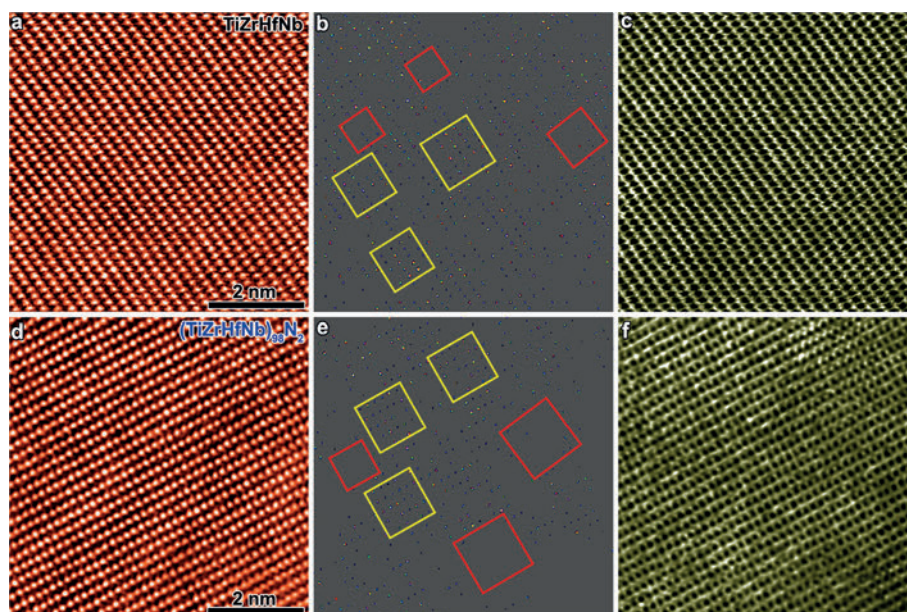
where  $3^{3/2}$  is a conversion factor between shear stress and hardness. The Young’s modulus of the base HEA is  $110.2 \pm 7.9$  GPa, obtained from nanoindentation measurements and the shear modulus was calculated to be 42.4 GPa. Based on these parameters, the calculated values of the tetragonal distortion  $\Delta\epsilon$  for the O-2 and N-2 HEAs are 0.10 and 0.14, respectively. These values are comparable to those of other tetragonal lattice distortions at room temperature<sup>53</sup>, indicating that the hardening mechanism in the current alloys is indeed of interstitial nature. The larger atomic size of nitrogen (atomic radius of 0.75 Å) compared to that of oxygen (0.65 Å) causes a higher asymmetry of the tetragonal distortions, thus leading to a larger  $\Delta\epsilon$  value and hence more pronounced interstitial strengthening. Via extrapolation from the synchrotron XRD data, the lattice parameter of the base, O-2 and N-2 HEAs was estimated to be 3.4308 Å, 3.4331 Å and 3.4347 Å, respectively, which confirms that the lattice distortion associated with adding nitrogen is indeed larger than that introduced when adding oxygen (Extended Data Fig. 10). As expected by conventional interstitial strengthening theory<sup>54–62</sup>, the interstitial strengthening always suffers from the strength–ductility trade-off (that the increase in strength leads to decreasing ductility). Nevertheless, addition of oxygen in the current b.c.c. HEA successfully reverses the strength–ductility trade-off.

## Data availability

The data that support the findings of this study are available from the corresponding authors on reasonable request.

33. Granberg, F. et al. Mechanism of radiation damage reduction in equiatomic multicomponent single phase alloys. *Phys. Rev. Lett.* **116**, 135504 (2016).
34. Zhang, Z. et al. Nanoscale origins of the damage tolerance of the high-entropy alloy CrMnFeCoNi. *Nat. Commun.* **6**, 10143 (2015).

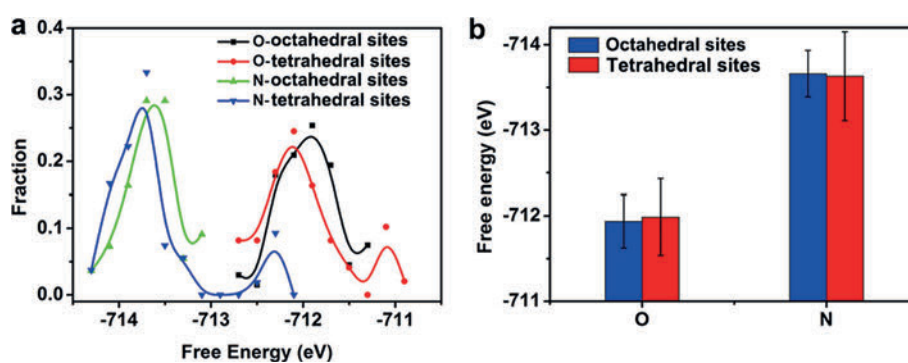
35. Zhang, Y. et al. Influence of chemical disorder on energy dissipation and defect evolution in concentrated solid solution alloys. *Nat. Commun.* **6**, 8736 (2015).
36. Zou, Y., Ma, H. & Spolenak, R. Ultrastrong ductile and stable high-entropy alloys at small scales. *Nat. Commun.* **6**, 7748 (2015).
37. Senkov, O. N. et al. Microstructure and elevated temperature properties of a refractory TaNbHfZrTi alloy. *J. Mater. Sci.* **47**, 4062–4074 (2012).
38. Gorr, B. et al. Phase equilibria, microstructure, and high temperature oxidation resistance of novel refractory high-entropy alloys. *J. Alloys Compd.* **624**, 270–278 (2015).
39. Wu, Y. D. et al. A refractory Hf<sub>25</sub>Nb<sub>25</sub>Ti<sub>25</sub>Zr<sub>25</sub> high-entropy alloy with excellent structural stability and tensile properties. *Mater. Lett.* **130**, 277–280 (2014).
40. Thompson, K. et al. In situ site-specific specimen preparation for atom probe tomography. *Ultramicroscopy* **107**, 131–139 (2007).
41. An, K. *VDRIVE-Data Reduction and Interactive Visualization Software for Event Mode Neutron Diffraction*. ORNL Report No. ORNL-TM-2012-621 (Oak Ridge National Laboratory, Oak Ridge, 2012).
42. Grandini, C. R. A low cost automatic system for anelastic relaxations measurements. *Rev. Brasil. Apl. Vácuo* **21**, 13–16 (2008).
43. Nowick, A. S. *Anelastic Relaxation in Crystalline Solids* Vol. 1 (Elsevier, New York, 2012).
44. Kresse, G. & Furthmüller, J. Efficient iterative schemes for ab initio total-energy calculations using a plane-wave basis set. *Phys. Rev. B* **54**, 11169 (1996).
45. Kresse, G. & Joubert, D. From ultrasoft pseudopotentials to the projector augmented-wave method. *Phys. Rev. B* **59**, 1758 (1999).
46. Perdew, J. P., Burke, K. & Ernzerhof, M. Generalized gradient approximation made simple. *Phys. Rev. Lett.* **77**, 3865 (1996).
47. Zunger, A., Wei, S. H., Ferreira, L. & Bernard, J. E. Special quasirandom structures. *Phys. Rev. Lett.* **65**, 353 (1990).
48. Press, W. H. *The Art of Scientific Computing* (Cambridge Univ. Press, New York, 1992).
49. Blöchl, P. E., Jepsen, O. & Andersen, O. K. Improved tetrahedron method for Brillouin-zone integrations. *Phys. Rev. B* **49**, 16223 (1994).
50. Methfessel, M. & Paxton, A. High-precision sampling for Brillouin-zone integration in metals. *Phys. Rev. B* **40**, 3616 (1989).
51. Courtney, T. H. *Mechanical Behaviour of Materials* (Waveland Press, New York, 2005).
52. Schuh, C. A., Nieh, T. G. & Iwasaki, H. The effect of solid solution W additions on the mechanical properties of nanocrystalline Ni. *Acta Mater.* **51**, 431–443 (2003).
53. Mitchell, T. E. & Heuer, A. H. Solution hardening by aliovalent cations in ionic crystals. *Mater. Sci. Eng. A* **28**, 81–97 (1977).
54. Finlay, W. L. & Snyder, J. A. Effects of three interstitial solutes (nitrogen, oxygen, and carbon) on the mechanical properties of high-purity, alpha titanium. *J. Met.* **2**, 277–286 (1950).
55. Ulitschny, M. & Gibala, R. The effects of interstitial solute additions on the mechanical properties of niobium and tantalum single crystals. *J. Less Common Met.* **33**, 105–116 (1973).
56. Šob, M., Kratochvíl, J. & Kroupa, F. Theory of strengthening of alpha titanium by interstitial solutes. *Czech. J. Phys.* **25**, 872–890 (1975).
57. Nakada, Y. & Keh, A. S. Solid-solution strengthening in Ni-C alloys. *Metall. Trans.* **2**, 441–447 (1971).
58. Nakada, Y. & Keh, A. S. Solid solution strengthening in Fe-N single crystals. *Acta Metall.* **16**, 903–914 (1968).
59. Li, Y. J., Ponge, D., Choi, P. & Raabe, D. Segregation of boron at prior austenite grain boundaries in a quenched martensitic steel studied by atom probe tomography. *Scr. Mater.* **96**, 13–16 (2015).
60. Kim, M., Geller, C. B. & Freeman, A. J. The effect of interstitial N on grain boundary cohesive strength in Fe. *Scr. Mater.* **50**, 1341–1343 (2004).
61. San Marchi, C. et al. in *Proc. 2008 International Hydrogen Conf.* 88–96 (ASM International, Russell Township, 2008).
62. Dadfarnia, M. et al. Recent advances in the study of structural materials compatibility with hydrogen. *Adv. Mater.* **22**, 1128–1135 (2010).
63. Snoek, J. Effect of small quantities of carbon and nitrogen on the elastic and plastic properties of iron. *Physica* **8**, 711–733 (1941).
64. Nelson, J. B. & Riley, D. An experimental investigation of extrapolation methods in the derivation of accurate unit-cell dimensions of crystals. *Proc. Phys. Soc.* **57**, 160 (1945).



**Extended Data Fig. 1 | Aberration-corrected STEM of the as-cast HEAs.** Shown are the HAADF-STEM images for the  $[011]_{\text{b.c.c.}}$  crystal axis with differently adjusted contrasts to show the existence of chemical short-range ordering, and the corresponding STEM-ABF images, for the equiatomic TiZrHfNb high-entropy base alloy (a–c) and for N-2 HEA

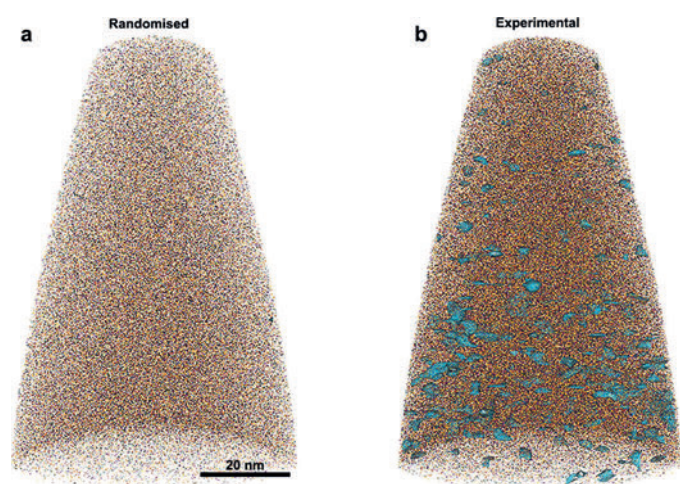
(that is,  $(\text{TiZrHfNb})_{98}\text{N}_2$ ) (d–f). The red panel represents the Zr/Ti-rich region, while the yellow panel indicates the Hf/Nb-rich region. No ordered interstitial occupation is observed in these two HEAs. Red squares represent the Zr/Ti-rich region and yellow squares indicate the Hf/Nb-rich region.





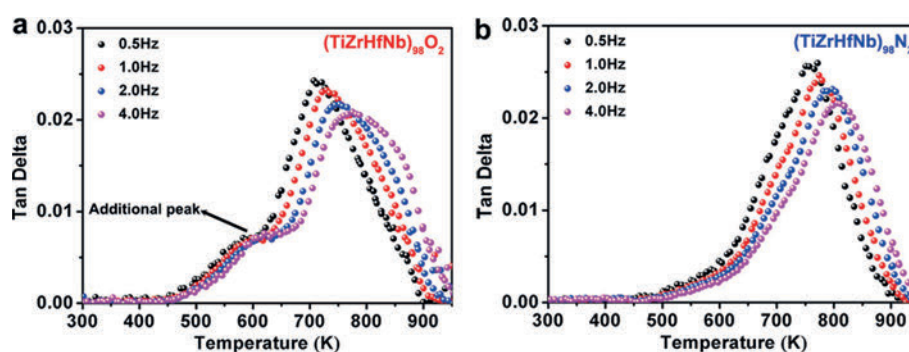
**Extended Data Fig. 2 | Occupation possibility analysis of interstitial oxygen/nitrogen from first-principles calculations.** **a**, Statistical distribution of system energy for the case of oxygen/nitrogen at different interstitial sites in the TiZrHfNb HEA. **b**, Comparison of average free energy for the systems with oxygen/nitrogen atoms at octahedral and tetrahedral interstitial sites. It can be seen that the octahedral interstitial

oxygen/nitrogen has a free energy nearly identical to that of the tetrahedral interstitial oxygen/nitrogen, indicating that the likelihood of oxygen/nitrogen atoms occupying the tetrahedral or octahedral interstitial sites in the b.c.c. lattice is similar. The error bars represent the standard error of the mean.



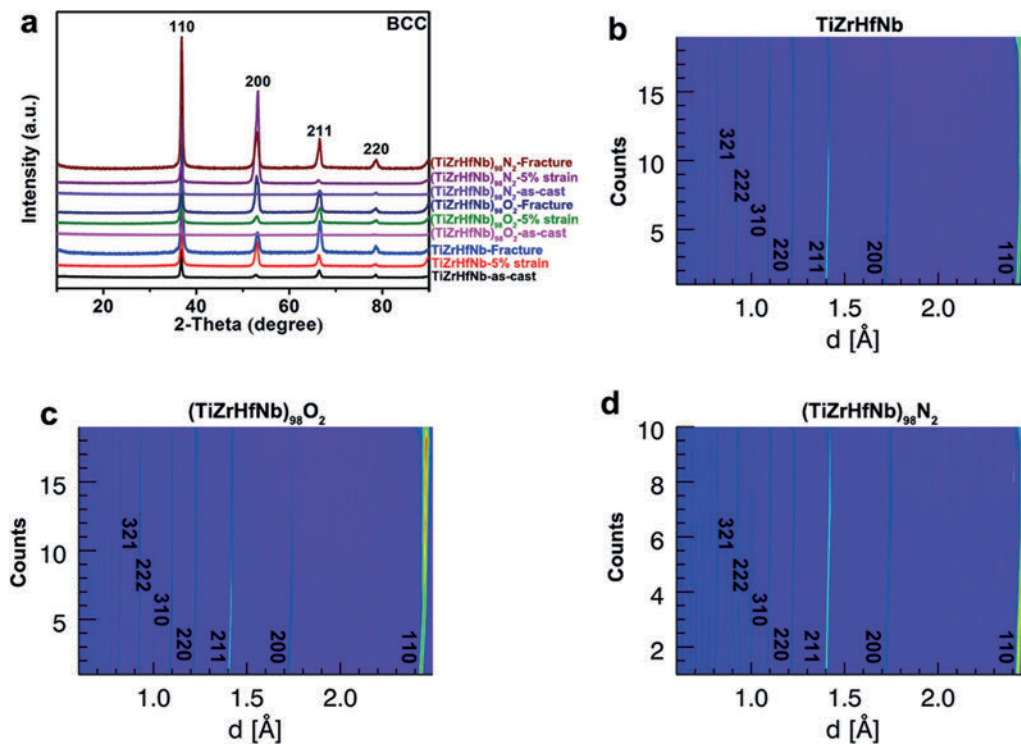
**Extended Data Fig. 3 | Three-dimensional reconstruction of the O-2 HEA atom probe tomography dataset. a, b, Randomized (a) and experimental (b) datasets on which an iso-composition surface encompassing regions in the point cloud containing more than 3.0 at% O was superimposed. The experimental dataset clearly shows evidence for OOCs.**





**Extended Data Fig. 4 | Internal-friction measurements.** Internal-friction results obtained for the O-2 (that is,  $(\text{TiZrHfNb})_{98}\text{O}_2$ ) and N-2 (that is,  $(\text{TiZrHfNb})_{98}\text{N}_2$ ) HEAs. Metals containing solute atoms in interstitial solution show Snoek relaxation behaviour owing to stress-induced ordering<sup>43</sup>, which gives rise to a peak in the corresponding internal-friction spectrum (that is, the Snoek peak)<sup>63</sup>, and different internal-friction peaks correspond to different types of local atomic environments

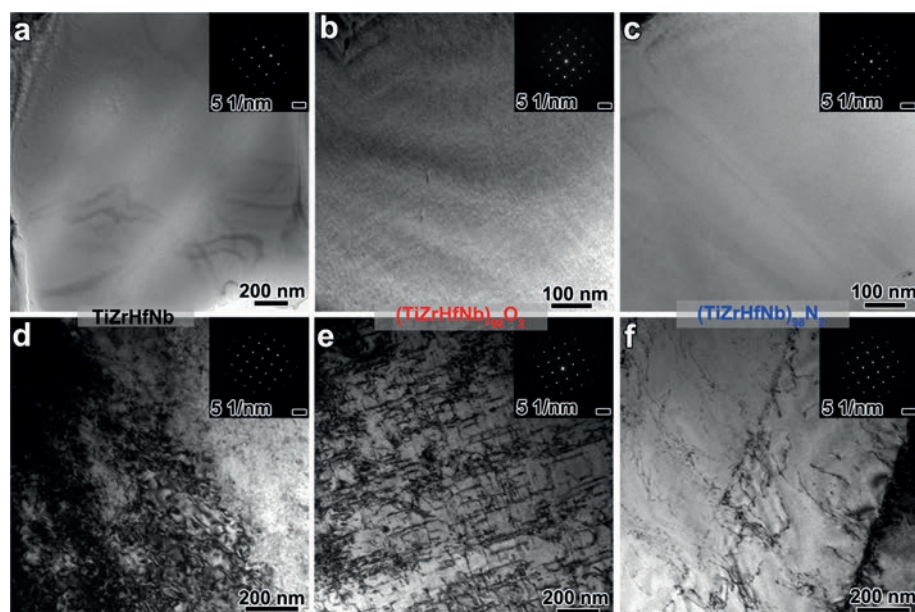
of the interstitials. Tan Delta represents the damping capacity. **a**, For the oxygen-doped alloy  $(\text{TiZrHfNb})_{98}\text{O}_2$  two peaks are observed: a dominant high-temperature peak and an additional low-temperature peak. **b**, For the nitrogen-doped alloy  $(\text{TiZrHfNb})_{98}\text{N}_2$  only the main peak is observed. This observation suggests that addition of oxygen to the TiZrHfNb HEA induces formation of two different types of interstitial atomic structures, unlike in the N-2 HEA, where only a single solid-solution peak appears.



**Extended Data Fig. 5 | X-ray and in situ neutron diffraction measurements.** **a**, XRD patterns of the TiZrHfNb base alloy, O-2 HEA (that is, (TiZrHfNb)<sub>98</sub>O<sub>2</sub>) and N-2 HEA (that is, (TiZrHfNb)<sub>98</sub>N<sub>2</sub>) with different pre-tensioned strains. **b–d**, In situ neutron diffraction patterns

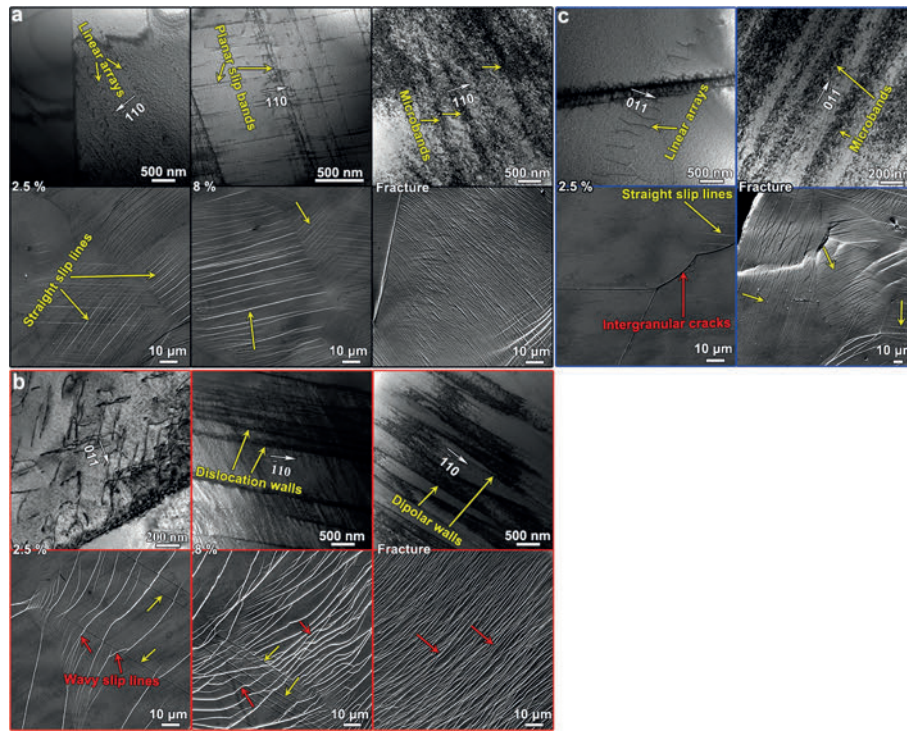
of the three alloys.  $d$  is the interplanar distance. Both ex situ XRD and in situ neutron diffraction measurements confirm that there is no phase transformation in the three HEAs during deformation.





**Extended Data Fig. 6 | Transmission electron microscopy.** **a–c**, TEM images of the as-cast equiatomic TiZrHfNb base alloy, O-2 HEA (that is,  $(\text{TiZrHfNb})_{98}\text{O}_2$ ) and N-2 HEA (that is,  $(\text{TiZrHfNb})_{98}\text{N}_2$ ). **d–f**, TEM images of the fractured HEA specimens. The TEM results further confirm

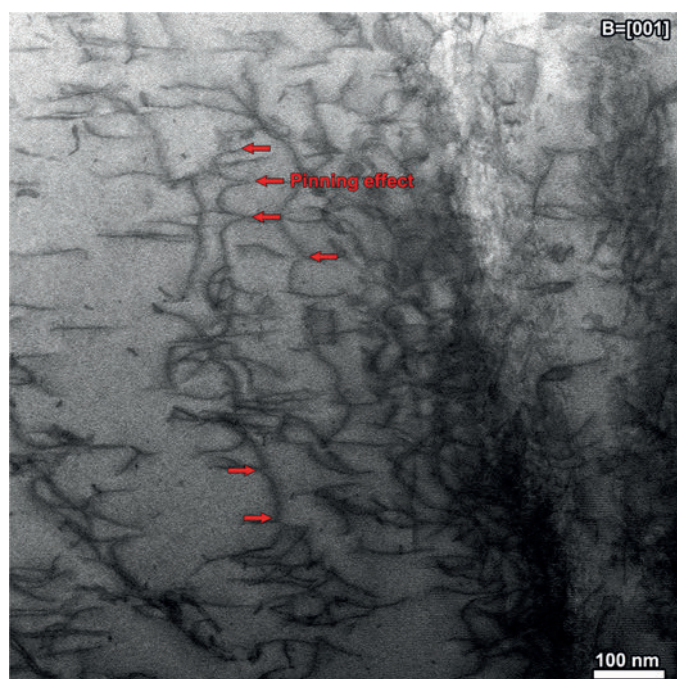
that no second phase appears before and after the tensile tests. The inset in each figure is the corresponding electron diffraction pattern of the selected area.



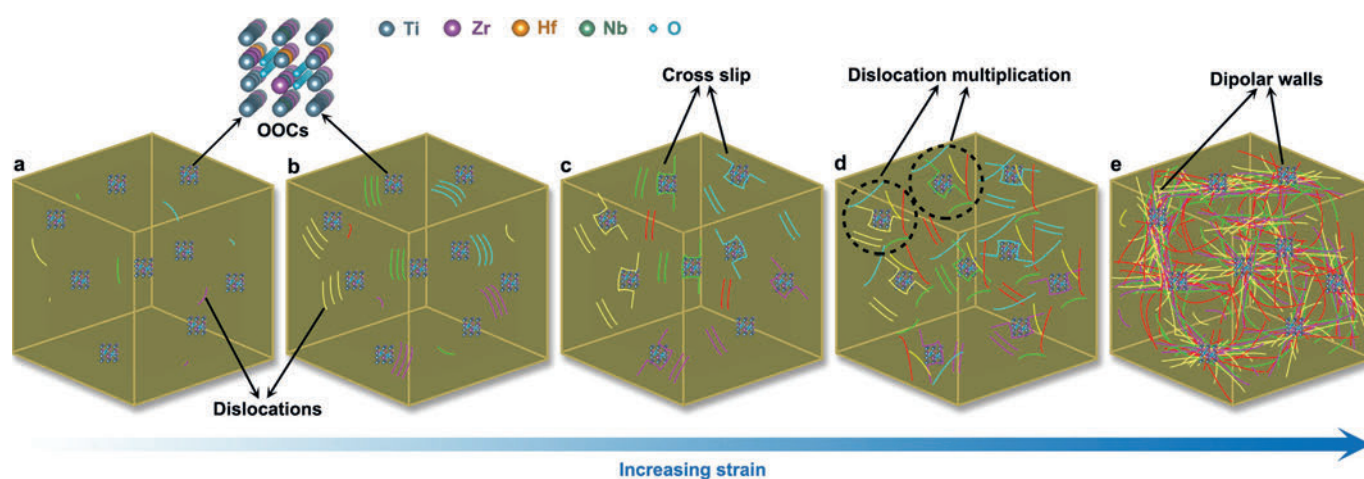
**Extended Data Fig. 7 | Dislocation configuration.** **a**, For the equiatomic TiZrHfNb base alloy, at low tensile strain (2.5% strain), dislocations in linear arrays are observed. As the strain increases to 8%, planar slip bands and individual dislocation-rich sheets are formed. After fracture, although irregular dislocation cells can be seen, there exist several microbands, indicating that planar slip is still the dominant deformation mode. **b**, For the oxygen-doped alloy variant O-2 HEA (that is, (TiZrHfNb)<sub>98</sub>O<sub>2</sub>) at 2.5% strain, however, the dislocations are arranged in bundles and loops. At 8% strain, dislocation walls are formed. For the dislocation substructure after fracture, dipolar walls that mainly contain primary dislocation dipoles at a high density are observed, suggesting a typical cell-forming

deformation microstructure in the O-2 HEA. **c**, For the nitrogen-doped alloy N-2 HEA (that is, (TiZrHfNb)<sub>98</sub>N<sub>2</sub>), the deformation mode is similar to that of the base alloy. In addition, slip traces at each specimen surface during deformation are also observed. Even at a low strain (2.5% strain), wavy slip lines are clearly seen in the oxygen doped variant O-2 HEA, whereas in the TiZrHfNb base alloy, even at high strain (8%), straight slip lines prevail and wavy slip lines only occur upon necking. Moreover, premature and much more serious necking occurs in the TiZrHfNb base alloy. It is worth mentioning here that intergranular fracture is observed in the nitrogen-doped variant N-2 HEA, which is probably caused by grain boundary segregation of nitrogen.

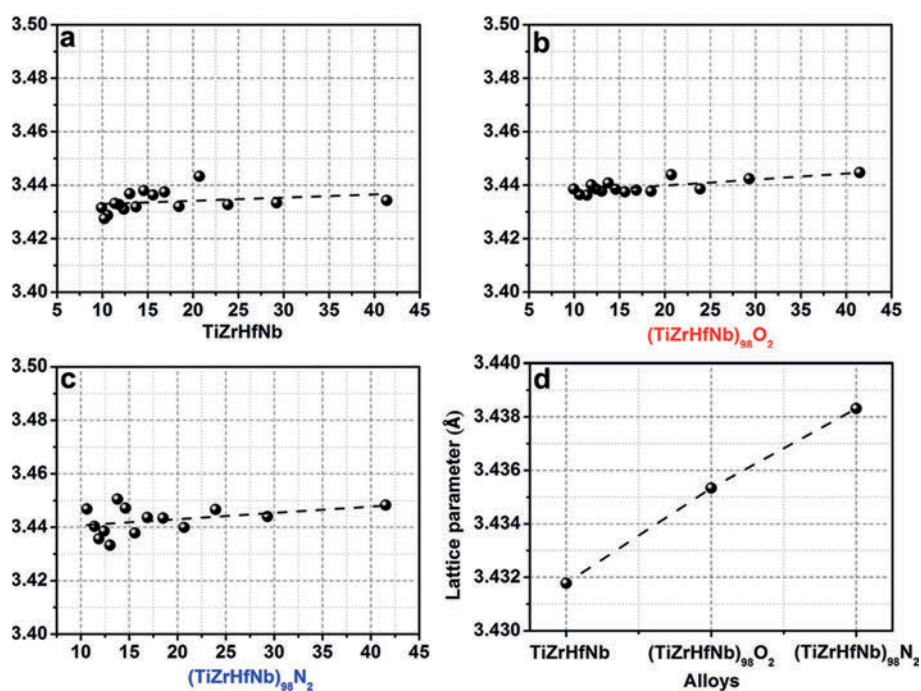




**Extended Data Fig. 8 | Pinning effect.** Aberration-corrected STEM observation of O-2 HEA (that is, (TiZrHfNb)<sub>98</sub>O<sub>2</sub>) after being pre-strained to 8%.  $B$  is the beam direction. The red arrows indicate the distinct dislocation pinning effect, which suppresses dislocation motion substantially during deformation.



Extended Data Fig. 9 | Schematic diagram illustrating the plastic deformation mechanism in the oxygen-rich alloy variant O-2 HEA.



**Extended Data Fig. 10 | Lattice parameter calculation.** a–c, Plot of measured values of the lattice parameter versus  $\frac{\cos^2 \vartheta}{2} \left( \frac{1}{\sin \vartheta} + \frac{1}{\vartheta} \right)$  for TiZrHfNb, (TiZrHfNb)<sub>98</sub>O<sub>2</sub> and (TiZrHfNb)<sub>98</sub>N<sub>2</sub> alloys. The position of each peak was measured on the diffractogram from which the lattice parameter was calculated. The measured lattice parameters were plotted

versus  $\frac{\cos^2 \vartheta}{2} \left( \frac{1}{\sin \vartheta} + \frac{1}{\vartheta} \right)$ , where  $\vartheta$  is the Bragg angle for each peak and the resulting graph extrapolated to zero to obtain the best value of the lattice parameter<sup>64</sup>. d, The calculated lattice parameters of the three alloys.